

# Supplementary information

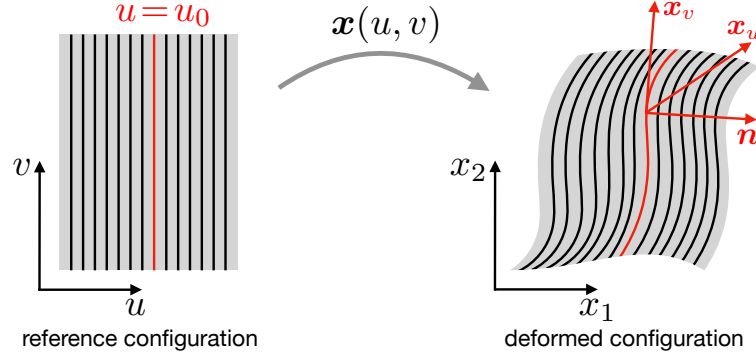
## Contents

<b>Supplementary Note 1</b>	
<b>Theory relating pellicle strip geometry and inter-strip sliding</b>	<b>2</b>
<b>Supplementary Note 2</b>	
<b>Estimation of friction coefficient and hydraulic resistance in the capillary</b>	<b>4</b>
<b>Supplementary Note 3</b>	
<b>Feasibility of flagellar locomotion in capillary confinement</b>	<b>7</b>
<b>Supplementary Note 4</b>	
<b>Theoretical model of the power phase of metaboly</b>	<b>8</b>
<b>Supplementary Note 5</b>	
<b>Computational model of confined crawling</b>	<b>11</b>
<b>Supplementary Note 6</b>	
<b>Confined metaboly in <i>Distigma proteus</i> and <i>Peranema trichophorum</i></b>	<b>18</b>
<b>Captions of Supplementary Movies</b>	<b>19</b>
<b>Supplementary References</b>	<b>21</b>

## Supplementary Note 1

### Theory relating pellicle strip geometry and inter-strip sliding

We particularize to the observations in Fig. 1(b) a previously developed theory relating the sliding between adjacent strips and the pellicle configuration [7, 18]. We consider the deformation of a planar region of pellicle with initially straight strips as shown in Supplementary Fig. 1. Because in the experiments in Fig. 1(b) cells are sandwiched between glass plates, the deformation of the imaged region of pellicle is such that it remains planar. We describe it mathematically by the mapping  $\mathbf{x}(u, v)$  from the plane to the plane, where  $v$  is a coordinate along the pellicle strips.



**Supplementary figure 1:** Sketch of the planar deformation of a region of pellicle. We consider an ideal reference configuration in which all pellicle strips are straight, which is deformed by the mapping  $\mathbf{x}$ .

According to the mechanism of deformation of the pellicle, this deformation is the result of a local shear deformation along the strips given by  $\gamma(u, v)$ . The relation between the deformation mapping  $\mathbf{x}$  and the pellicle shear distribution  $\gamma$  is given by the relations [7, 18]

$$1 + \gamma^2 = \mathbf{x}_u \cdot \mathbf{x}_u, \quad (1)$$

$$1 = \mathbf{x}_v \cdot \mathbf{x}_v, \quad (2)$$

$$\gamma = \mathbf{x}_u \cdot \mathbf{x}_v, \quad (3)$$

where  $\mathbf{x}_u$  and  $\mathbf{x}_v$  denote the partial derivatives of  $\mathbf{x}$  with respect to the coordinates  $u$  and  $v$ . Pellicle lines are given by  $u = u_0 = \text{constant}$  in the reference configuration and by  $\mathbf{x}(u_0, v)$  in the deformed configuration. Thus, the vector field  $\mathbf{x}_v$  is tangential to deformed pellicle lines. Furthermore, Eq. (2) shows that this vector field has unit length, and thus  $\mathbf{x}(u_0, v)$  is an arc-length parametrization of the deformed pellicle strip given by  $u = u_0$  (pellicle strips do not stretch). Since  $v$  is the arc-length parameter, the signed curvature of pellicle strips  $\kappa$  is given by the relation [36]

$$\mathbf{x}_{vv} = \kappa \mathbf{n}, \quad (4)$$

where  $\mathbf{n}$  is a unit vector field normal to the pellicle strips. An expression for the normal vector can be obtained by subtracting to  $\mathbf{x}_u$  its projection along  $\mathbf{x}_v$ , see Supplementary Fig. 1,

$$\mathbf{n} = \mathbf{x}_u - (\mathbf{x}_u \cdot \mathbf{x}_v) \mathbf{x}_v = \mathbf{x}_u - \gamma \mathbf{x}_v, \quad (5)$$

where we have used Eq. (3). Note that  $|\mathbf{n}|^2 = \mathbf{n} \cdot \mathbf{n} = \mathbf{x}_u \cdot \mathbf{x}_u - 2\gamma \mathbf{x}_u \cdot \mathbf{x}_v + \gamma^2 \mathbf{x}_v \cdot \mathbf{x}_v = 1$ , where we have used Eqs. (1–3). We conclude that

$$\mathbf{x}_{vv} = \kappa (\mathbf{x}_u - \gamma \mathbf{x}_v). \quad (6)$$

To find an alternative expression for the vector  $\mathbf{x}_{vv}$ , we express it in the basis formed by  $\mathbf{x}_u$  and  $\mathbf{x}_v$  as

$$\mathbf{x}_{vv} = a \mathbf{x}_u + b \mathbf{x}_v. \quad (7)$$

Differentiation of the Eq. (2) with respect to  $u$  and  $v$  leads to

$$0 = \mathbf{x}_v \cdot \mathbf{x}_{uv}, \quad (8)$$

$$0 = \mathbf{x}_v \cdot \mathbf{x}_{vv}. \quad (9)$$

Differentiation of the Eq. (3) with respect to  $v$  leads to

$$\gamma_v = \mathbf{x}_u \cdot \mathbf{x}_{vv} + \mathbf{x}_v \cdot \mathbf{x}_{uv} = \mathbf{x}_u \cdot \mathbf{x}_{vv}, \quad (10)$$

where we have used Eq. (8) in the second step. Thus, combining Eqs. (7, 9, 10) we find

$$\gamma_v = \mathbf{x}_u \cdot \mathbf{x}_{vv} = (1 + \gamma^2)a + \gamma b, \quad (11)$$

$$0 = \mathbf{x}_v \cdot \mathbf{x}_{vv} = \gamma a + b. \quad (12)$$

Inverting these relations, we find that  $a = \gamma_v$  and  $b = -\gamma\gamma_v$ , and thus

$$\mathbf{x}_{vv} = \gamma_v (\mathbf{x}_u - \gamma \mathbf{x}_v). \quad (13)$$

Comparing this expression with Eq. (6), we conclude that

$$\gamma_v = \kappa, \quad (14)$$

which coincides with the expression in Fig. 1(d) denoting  $v$  by  $s$ .

To compute relative sliding displacements from this expression, we considered pellicle strips emanating from the anterior end (given by  $s = 0$ ), where strips converge and cannot slide relative to each other,  $\gamma(s = 0) = 0$ . We then fitted spline curves to such strips and computed their curvature as a function of arc-length  $\kappa(s)$  at selected time instants. The sliding displacement required to bend an initially straight strip to the observed configuration is then

$$w\gamma(s) = w \int_0^s \kappa(r) dr, \quad (15)$$

computed as the product of the shear strain and the width of a strip  $w$ .

## Supplementary Note 2

### Estimation of friction coefficient and hydraulic resistance in the capillary

Biological locomotion at microscopic scales is the result of forces exerted by the environment on the cell surface. For an *Euglena* cell under capillary confinement, these forces are exerted on the pellicle by the fluid in the capillary and by the capillary walls. Hydrodynamic forces are essentially those required to displace the column of water in the capillary as the cell moves. Since *Euglena* are not known to establish specific adhesions with substrates, we reasoned that the mechanical interaction with the capillary wall should include contact forces normal to it, and thus not directly contributing to propulsion, and tangential forces due to unspecific viscous friction and thus proportional to the sliding velocity, in agreement with previous reports on animal cells [24] and with the framework of hydration lubrication [37], which studies the rheological properties of thin aqueous interfaces such as those between cells and solid substrates.

To understand and quantify the forces experienced by a non-deforming cell moving under capillary confinement, we drove cells into the narrower sections of capillaries. Tapered glass capillaries of circular cross section were filled with a diluted solution of cells and of 1  $\mu\text{m}$  polystyrene, fluorescent beads ( $\sim 1.5 \text{ mg/mL}$  from Life Technologies, catalog number F8823) in culture medium (CM) Eg. The capillaries were then fixed to the microscope stage by means of a custom made, 3d-printed holder and their inlet was connected to an external reservoir of CM. The holder was designed in such a way that the capillaries were positioned between two 0.17 mm coverslips and immersed in CM. Starting from a state of hydrostatic equilibrium, lifting the external reservoir resulted in a controlled increase of the pressure (relative to the reference atmospheric pressure) at the capillary inlet,  $p_{\text{in}}$ , and in fluid flow within it. Eventually, a cell convected by the flow contacted the capillary wall and created a hydraulic seal. This condition was verified by the imaging of micro-beads diluted in the solution, whose velocity correlated with that of the cell and which stopped when cells became immobile, Supplementary Movie S7. Consequently, under these conditions cell velocity was a reporter of the flow rate in the capillary. Note that in a Poiseuille flow, beads can go faster or slower than the average flow velocity given by that of the cells.

The cell motion along the capillary axis was recorded at 40 fps with a Basler digital camera (model acA2000-50gm) and an Olympus Plan N 10X objective (NA 0.25). Analysis of the micrographs allowed us to determine the cell position along the capillary  $x_{\text{cell}}$ , its radius, which coincides with the capillary radius at the cell position  $r(x_{\text{cell}})$ , the cell velocity  $v_{\text{cell}}$ , and the length of the contact area  $\ell_c$ .

Inertia being negligible in these experiments, the net forces due to pressure differences across a cell  $\delta p$  and given by

$$F_{\text{fluid}} = \delta p \pi r^2, \quad (16)$$

had to be balanced by the frictional forces between the cell and the capillary, which we modeled as

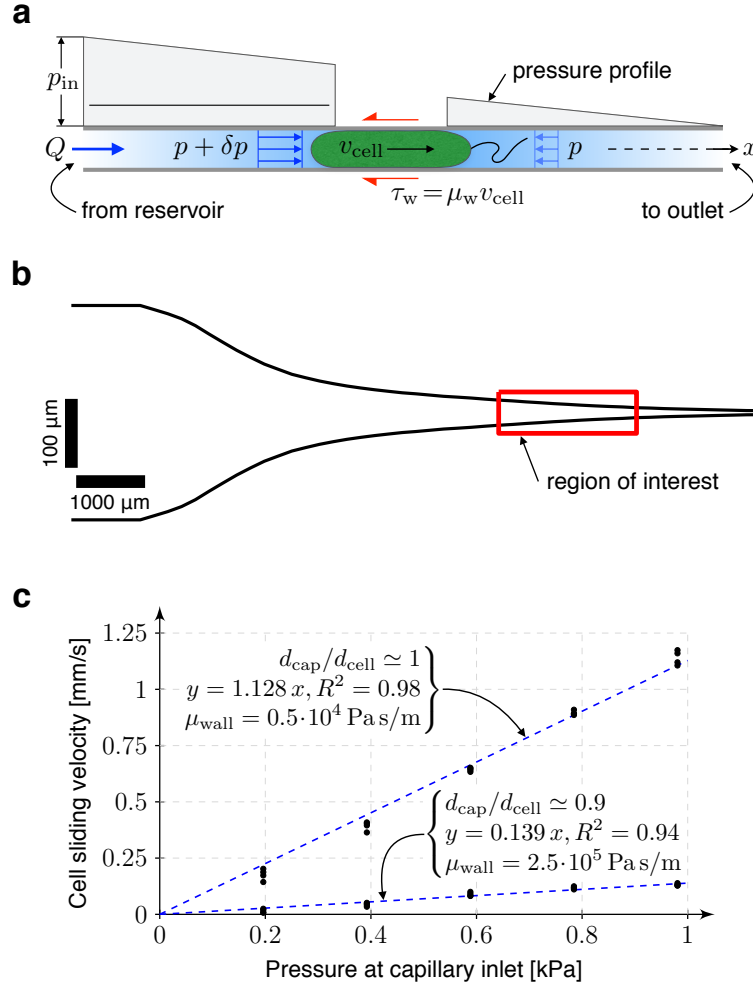
$$F_{\text{wall}} = -2\pi r \ell_c \mu_{\text{wall}} v_{\text{cell}} \quad (17)$$

where  $\mu_{\text{wall}}$  is a viscous friction coefficient linearly relating sliding velocity, which here coincides with the cell velocity, and the frictional force per unit area  $\tau_{\text{wall}} = \mu_{\text{wall}} v_{\text{cell}}$ , Supplementary Fig. 2(a). By balancing these two forces, we found

$$\delta p = \frac{2\ell_c}{r} \mu_{\text{wall}} v_{\text{cell}}. \quad (18)$$

The pressure jump across the cell  $\delta p$  could also be estimated with elementary hydrodynamics. Assuming a Poiseuille flow and small capillary taper ( $dr/dx \ll 1$ ) leads to

$$\frac{dp}{dx} = -\frac{8\eta}{\pi r^4} Q, \quad (19)$$



**Supplementary figure 2: Estimation of friction coefficient and hydraulic resistance in the capillary.** (a) Force balance for a confined cell moving in a capillary by a pressure difference. (b) profile of a typical pulled capillary. (c) Linear relation between the cell velocity and the applied pressure, allowing us to measure the friction coefficient  $\mu_{\text{wall}}$ . We performed four measurements from the same sample for each condition (confinement and applied pressure). We performed analogous measurements for other cells.

where  $\eta$  is the dynamic viscosity of the solvent and  $Q = \pi r^2 v_{\text{cell}}$  is the flow rate. The pressure difference across the cell,  $\delta p$ , was determined by integration of the equation above while accounting for the boundary conditions on pressure at inlet and outlet (where  $p = 0$ ), leading to

$$\delta p = p_{\text{in}} - \frac{\zeta}{\pi} Q, \quad (20)$$

where

$$\zeta = 8\eta \left( \int_0^{x_{\text{cell}} - \ell_c/2} r^{-4} dx + \int_{x_{\text{cell}} + \ell_c/2}^L r^{-4} dx \right) \approx 8\eta \int_0^L r^{-4} dx, \quad (21)$$

is the the hydraulic resistance and  $L$  the capillary length. We computed this quantity for the actual geometry of the capillaries as measured from the micrographs, Supplementary Fig. 2(b), obtaining  $\zeta = 5 \cdot 10^{16} \text{ N s/m}^5$ .

Equating the two expressions for  $\delta p$ , we obtained the following linear relation between cell velocity and pressure applied at the inlet

$$p_{\text{in}} = \left( \frac{2\ell_c}{r} \mu_{\text{wall}} + r^2 \zeta \right) v_{\text{cell}}. \quad (22)$$

Since the coefficient  $\mu_{\text{wall}}$  could depend on the lateral confining pressure, we considered the possibility that it could be confinement-dependent. For this reason,  $\mu_{\text{wall}}$  could be considered as constant in the equation above, provided that measurements were performed at a given position in the capillary  $x$  with radius  $r(x)$ . To test this relationship, we carried out tests for different values of  $p_{\text{in}}$  and measured cell velocity at specified positions (and thus specified degrees of confinement). Consistent with our model, we found a confinement-dependent linear relationship between inlet pressure and cell velocity, Supplementary Fig. 2(c), which allowed us to measure the ratio  $p_{\text{in}}/v_{\text{cell}}$  and thereby the confinement-dependent friction coefficient  $\mu_{\text{wall}}$ . Indeed, rearranging Eq. (22) we have

$$\mu_{\text{wall}} = \frac{r}{2\ell_c} \left( \frac{p_{\text{in}}}{v_{\text{cell}}} - r^2\zeta \right). \quad (23)$$

Our measurements for the friction coefficient were in the range of  $10^4 - 10^5$  Pa s/m, comparable to those reported between animal cells and PDMS channels [24].

## Supplementary Note 3

### Feasibility of flagellar locomotion in capillary confinement

From the typical speed of free-swimming cells,  $v_{\text{free}} \simeq 68 \mu\text{m/s}$ , and approximating their body geometry by prolate spheroids of semi-major and semi-minor axis  $a \simeq 25 \mu\text{m}$  and  $b \simeq 4.5 \mu\text{m}$  to compute the drag coefficient, we estimated the flagellar propulsive force to be

$$F_p = 6\pi\eta a v_{\text{free}} \chi(e) \simeq 10.9 \text{ pN}, \quad (24)$$

where

$$\chi(e) = \frac{8e^3}{3[(1+e^2)\log[(1+e)/(1-e)] - 2e]} \quad (25)$$

is a coefficient accounting for the spheroid eccentricity,  $e = [1 - (b/a)^2]^{1/2}$  [38].

Assuming that a cell could exert the same propulsive force in capillary confinement, in order to move forward it would need to overcome the hydraulic resistive force  $F_{\text{fluid}}$  required to move the column of water in the capillary and the frictional force  $F_{\text{wall}}$ . Adapting the model of the Supplementary Note 2, we have

$$F_{\text{fluid}} = -8\pi\eta r^4 v_{\text{cell}} \int_0^L r^{-4} dx = -\pi\zeta r^4 v_{\text{cell}}, \quad (26)$$

where  $\zeta \simeq 5 \cdot 10^{16} \text{ N s/m}^5$  is defined in Eq. (21), and

$$F_{\text{wall}} = -2\pi r \ell_c \mu_{\text{wall}} v_{\text{cell}}. \quad (27)$$

Force balance during flagellar locomotion requires that  $F_p + F_{\text{fluid}} + F_{\text{wall}} = 0$ , and thus

$$F_p = -F_{\text{fluid}} - F_{\text{wall}} = \pi(\zeta r^4 + 2r\ell_c\mu_{\text{wall}}) v_{\text{cell}}, \quad (28)$$

which allows us to estimate the velocity at which a cell would move in capillary confinement while propelled by flagella. We considered a first situation of moderate confinement ( $d_{\text{cap}}/d_{\text{cell}} \approx 1$ ), with  $r = 4.5 \mu\text{m}$ ,  $\ell_c = 10 \mu\text{m}$  and  $\mu_{\text{wall}} = 0.5 \cdot 10^4 \text{ Pa s/m}$ , which led to  $v_{\text{cell}} \sim 0.15 \mu\text{m/s}$ , about 10 times smaller than the crawling velocity by metaboly at this degree of confinement, Fig. 2(c). We then considered a more confined case with  $r = 4 \mu\text{m}$ ,  $\ell_c = 30 \mu\text{m}$  and  $\mu_{\text{wall}} = 2.5 \cdot 10^5 \text{ Pa s/m}$ , which led to  $v_{\text{cell}} \sim 0.05 \mu\text{m/s}$ , about 20 times smaller than the crawling velocity by metaboly at this degree of confinement.

## Supplementary Note 4

### Theoretical model of the power phase of metaboly

During metaboly, a power phase corresponding to a bulge of fixed shape traveling along the body in direction opposite to that of the resulting crawling motion can be clearly identified, see Supplementary Movie 6 and Figs. 2 and 3. A simplified model of this process can be derived by assuming that the strips in the thinner cylindrical end sections are all aligned with the main body axis, and that the angle  $\theta^*$  between strips in the bulge and that axis is constant in the region in contact with the capillary. We note that allowing strips in the thinner section of the cell body to be helical slightly complicates the mathematical expressions but does not fundamentally alter the conclusions. The transition between the wider cylindrical bulge, of radius  $r$ , and the thinner cylindrical end sections, of radius  $r_0$ , can be realized by modulating the pellicle shear from the maximal value  $\gamma^*$  at the bulge, and the reference value  $\gamma = 0$  at the ends, provided that the transition region is sufficiently long [18]. The bulge is assumed to be in contact with the capillary walls in a region of length  $\ell_c$ , establishing a hydraulic plug which does not allow transfer of fluid between the regions ahead of and behind the cell. See Fig. 3(b) and Supplementary Fig. 3 for an illustration. Elementary geometry shows that the radius of the slender part of the cell body, that of the bulge in contact with the capillary, and the angle  $\theta^*$  follow the relation [18]

$$r_0 = r \cos \theta^*. \quad (29)$$

To analyze the kinematics and mechanics of this idealized gait, we define three frames of reference, the laboratory frame where the capillary is quiescent, whose origin is  $O$ , the frame of the cell fixed for instance at the leading edge of the cell ( $O_{\text{tip}}$ ), and a frame attached to a fixed material point ( $O_{\text{contact}}$ ) in the region of the bulge in contact with the wall, see Supplementary Fig. 3. We assume that the bulge is generated by a traveling localized profile of active shear given by  $\gamma(s, t) = \bar{\gamma}(s - ct)$ , where  $c$  is the velocity of the actuation pattern along the coordinate  $s$  describing arc-length of strips, Fig. 3(b). We adopt the convention that all velocities are positive when they represent motions from left to right. Since we consider backward moving bulges,  $c < 0$ . As a result of this motion of the activation pattern, the bulge also moves backwards at velocity  $c$  in the frame of the cell. In the frame attached to  $O_{\text{contact}}$ , however, the bulge moves slower at velocity  $c \cos \theta^*$  given the geometry of the bulge.

The other velocities characterizing the kinematics of the cell are

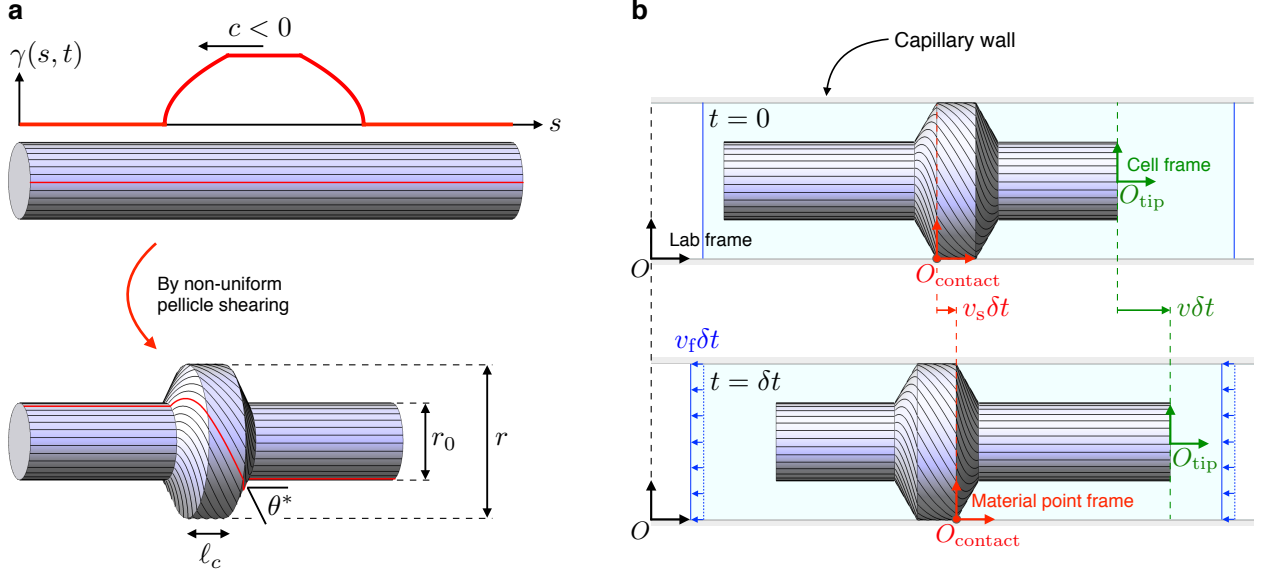
- the sliding velocity  $v_s$ , that is the velocity of  $O_{\text{contact}}$  relative to  $O$ ,
- the velocity of  $O_{\text{tip}}$  relative to  $O_{\text{contact}}$ ,  $dl/dt$ ,
- the cell velocity  $v$  in the laboratory frame, that is the velocity of  $O_{\text{tip}}$  relative to  $O$ ,
- the velocity of the bulge  $v_b$  in the laboratory frame (the velocity of the leading edge of the bulge relative to  $O$ ),
- the average fluid velocity  $v_f = Q/(\pi r^2)$  in the capillary at a small distance from the cell in the laboratory frame.

We assume  $c$  to be given, and obtain the other five unknown velocities from the kinematics of the traveling bulge and force balance. The forces acting on the cell are the frictional force exerted by the wall, which depends on the velocity of points in the contact region relative to the capillary wall

$$F_{\text{wall}} = -2\pi r \ell_c \mu_{\text{wall}} v_s, \quad (30)$$

and the hydraulic force exerted by the fluid

$$F_{\text{fluid}} = -\alpha Q = -\alpha \pi r^2 v_f, \quad \text{where } \alpha = \zeta r^2, \quad (31)$$



**Supplementary figure 3:** (a) Idealized model of the power phase of metaboly and (b) two snapshots of the resulting motion in a capillary to highlight the frames of reference relevant to the analysis and the three velocities  $v$ ,  $v_s$ , and  $v_f$ .

$\zeta$  is defined in (21), and the expression of  $F_{\text{fluid}}$  follows from (20) by assuming that inlet and outlet are at atmospheric pressure,  $p_{\text{in}} = p_{\text{out}} = 0$ . Force balance on the cell gives then

$$0 = F_{\text{wall}} + F_{\text{fluid}}. \quad (32)$$

Introducing the nondimensional parameter

$$\xi = \frac{2\mu_{\text{wall}}\ell_c}{\alpha r} \quad (33)$$

controlling the relative strength of friction and hydraulic resistance, force balance can be rewritten as

$$0 = \xi v_s + v_f. \quad (34)$$

From the previous definitions, we can express the velocity of the bulge in the laboratory frame in terms of its velocity relative to  $O_{\text{contact}}$  and the sliding velocity as

$$v_b = v_s + c \cos \theta^*. \quad (35)$$

Likewise, we can express the cell velocity relative to  $O$  as

$$v = v_s + \frac{dl}{dt}. \quad (36)$$

Furthermore, noting that the pellicle deformation mechanism locally preserves area, and thus the area of pellicle to the right (or left) of material point  $O_{\text{contact}}$  remains constant during the motion, we derive the following relation

$$0 = 2\pi(r - r_0)c \cos \theta^* + 2\pi r_0 \frac{dl}{dt}. \quad (37)$$

Finally, volume conservation of the fluid inside the capillary yields

$$\pi r^2 v_f = Q = \pi(r^2 - r_0^2)v_b + \pi r_0^2 v. \quad (38)$$

Solving the last five equations for the five unknown velocities we obtain

$$v_s = -\frac{1}{1+\xi}(1 - \cos \theta^*) \cos \theta^* c, \quad (39)$$

$$v_f = \frac{\xi}{1+\xi}(1 - \cos \theta^*) \cos \theta^* c, \quad (40)$$

$$v = -\left(1 + \frac{\cos \theta^*}{1+\xi}\right)(1 - \cos \theta^*) c, \quad (41)$$

$$v_b = \frac{\cos \theta^* + \xi}{1+\xi} \cos \theta^* c, \quad (42)$$

and

$$\frac{dl}{dt} = -(1 - \cos \theta^*) c. \quad (43)$$

In the limit of vanishing hydrodynamic resistance relative to the wall friction,  $\xi \rightarrow +\infty$ , we obtain

$$v = -(1 - \cos \theta^*) c, \quad v_s = 0, \quad v_f = (1 - \cos \theta^*) \cos \theta^* c. \quad (44)$$

In the opposite limit of vanishing wall friction relative to hydraulic resistance,  $\xi \rightarrow 0$ , we obtain instead

$$v = -(1 - \cos^2 \theta^*) c, \quad v_s = -(1 - \cos \theta^*) \cos \theta^* c, \quad v_f = 0. \quad (45)$$

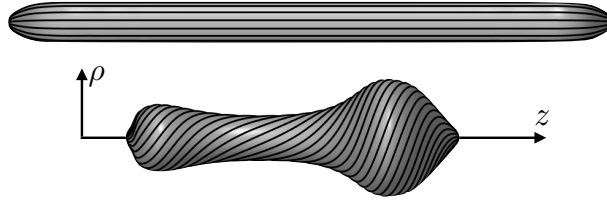
It is easy to see that, in the general case, the cell, sliding, and fluid velocities are intermediate between those of the two extreme situations.

## Supplementary Note 5

### Computational model of confined crawling

#### Setup

We describe mathematically the pellicle of euglenids as a deformable surface and focus on axisymmetric cells. We consider a reference configuration of the cell given by a surface  $\Gamma$  described by a parametrization of its generating curve  $\{\rho_0(u), z_0(u)\}$ ,  $u \in [0, 1]$ , not necessarily parametrized by arc-length. In this reference configuration, the pellicle strips are meridians of the axisymmetric surface, see Supplementary Fig. 4. A general deformed configuration of the cell at time  $t$  under the assumption of axisymmetry is defined by the deformed generating curve and the azimuthal angle displacement,  $\{\rho(u, t), z(u, t), \psi(u, t)\}$ . We denote space derivatives by  $\rho'$  and time derivatives by  $\dot{\rho}$ .



**Supplementary figure 4:** Reference pellicle surface  $\Gamma$  (top) and an axisymmetric deformed shape of the reference pellicle resulting from a nonuniform pellicle shear distribution (bottom).

The pellicle is an active surface, capable of undergoing simple shear along a Lagrangian direction given by the strips under the action of molecular motors. We denote the pellicle shear field relative to the reference configuration by  $\gamma(u, t)$ . Shape changes are the result of this actively generated deformation. The precise connection between deformation and pellicle shear can be established by noting that the (Cauchy-Green) deformation tensor of the surface can be expressed either as [7, 18]

$$\mathbf{C} = \begin{bmatrix} \frac{\rho'^2 + z'^2 + \rho^2 \psi'^2}{a_0^2} & \frac{\rho^2 \psi'}{\rho_0 a_0} \\ \frac{\rho^2 \psi'}{\rho_0 a_0} & \left(\frac{\rho}{\rho_0}\right)^2 \end{bmatrix}, \quad (46)$$

where  $a_0^2 = \rho_0'^2 + z_0'^2$ , or as

$$\bar{\mathbf{C}} = \begin{bmatrix} 1 & \gamma \\ \gamma & 1 + \gamma^2 \end{bmatrix}. \quad (47)$$

By equating these two forms of the same physical quantity, we obtain a set of algebraic and differential equations, which for instance allow us to compute  $\{\rho(u, t), z(u, t), \psi(u, t)\}$  given the internal actuation  $\gamma(u, t)$ .

While this geometric approach is very powerful to understand the pellicle kinematics, it has limitations in the present context. First, the resulting equations do not always admit solutions. If the pellicle shear  $\gamma$  is too large or has very sharp variations, as made precise elsewhere [18], it may not be “embeddable”, meaning that there exist no geometric realization of the pellicle having  $\bar{\mathbf{C}}$  as its deformation tensor. A way to make this set of kinematic relations more flexible, and also more physical, is to allow for some stretching of the surface, and elastically penalize deviations between  $\mathbf{C}$  and  $\bar{\mathbf{C}}$  as described below. Another limitation of trying to prescribe  $\gamma(u, t)$  directly is that, if an euglenid is performing metaboly in the presence of constraints such as the wall of a capillary, then the reaction forces associated with the constraints will oppose the action of the molecular motors and could even stall them. For this reason, rather than imposing the pellicle shear  $\gamma(u, t)$ , in the present model we impose a biological activity creating forces conjugate to pellicle sliding. We will then obtain  $\gamma(u, t)$ , now an unknown, as the result of balancing the externally applied forces on the motors with those being actively generated.

## Model ingredients

To model the mechanics depicted in Fig. 4(a), which couple elasticity, dissipative mechanisms, constraints and active power input, we resort to Onsager’s variational principle [39, 40], which, given the enumeration of the elastic and dissipation potentials describing the different physical mechanisms, provides a systematic tool to derive the governing mechanical equations by minimizing the Rayleighian functional. In this systematic modeling approach, it is important to formalize the state of the system, which here is given by the deformation of the pellicle and the actual pellicle shear distribution:

$$X(u, t) = \{\rho(u, t), z(u, t), \psi(u, t), \gamma(u, t)\}, \quad u \in [0, 1], t \geq 0.$$

We will derive equations to find the dynamics of these state variables.

## Elastic energy

To account for the elastic in-plane stretchability of the pellicle and without attempting to describe in detail the possibly anisotropic mechanical properties of the pellicle, we consider a Kirchhoff-Saint Venant energy, which locally penalizes deviations between the actual deformation and that given by  $\gamma(u, t)$ , along with a Helfrich energy contribution to elastically penalize curvature

$$\begin{aligned} E_{\text{elastic}}[\rho, z, \psi, \gamma] &= \frac{Y}{2} \int_{\Gamma} |\mathbf{C} - \bar{\mathbf{C}}|^2 dS_0 + \frac{D}{2} \int_{\Gamma} H^2 dS_0 \\ &= \frac{Y}{2} \int_{\Gamma} \left[ \left( \frac{\rho'^2 + z'^2 + \rho^2 \psi'^2}{a_0^2} - 1 \right)^2 + 2 \left( \frac{\rho^2 \psi'}{\rho_0 a_0} - \gamma \right)^2 + \left( \left( \frac{\rho}{\rho_0} \right)^2 - 1 - \gamma^2 \right)^2 \right] dS_0 \\ &\quad + \frac{D}{2} \int_{\Gamma} H^2 dS_0, \end{aligned}$$

where  $Y$  is the stretching modulus,  $D$  is a bending modulus,  $H$  is the mean curvature, and  $dS_0 = 2\pi\rho_0 a_0 du$ . Note that, because the pellicle surface is largely inextensible,  $dS_0$  is very close to  $dS$  and the last term closely approximates the usual Helfrich functional used to model lipid membranes.

## Volume conservation

At the typical time-scales of metaboly, our observations suggest that cells can be considered as incompressible. Without attempting to model the active and passive processes leading to cell volume regulation, we penalize volume variations with respect to a target volume  $\bar{V}$  by

$$E_{\text{volume}}[\rho, z] = \frac{K}{2} (V[\rho, z] - \bar{V})^2,$$

where  $V[\rho, z]$  is the cell volume, depending only on the parametrization of the generating curve, and  $K$  is a parameter large enough to control cell volume variations within a few percent.

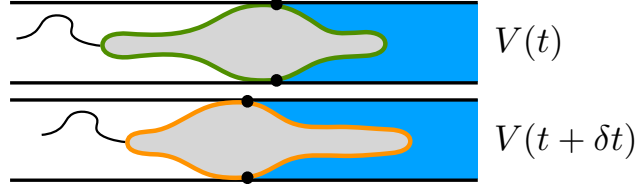
## Contact with a capillary wall

We model the contact interaction with a capillary wall with a potential  $\mathcal{V}(\rho)$  that becomes repulsive when  $\rho \geq r$ , the radius of the capillary. Here, we consider

$$\mathcal{V}(\rho) = \begin{cases} 0 & \text{if } \rho < r \\ \frac{k}{p} \left( \frac{\rho - r}{\delta} \right)^p & \text{if } \rho \geq r \end{cases}$$

where  $\delta$  is the “thickness” of the interaction. We take  $\delta \ll r$ ,  $p = 3$ , and the parameter  $k$  is large enough so that the maximum cell radius only exceeds  $r$  by a few percent. The resulting energy functional is

$$E_{\text{contact}}[\rho] = \int_{\Gamma} \mathcal{V}(\rho) dS_0.$$



**Supplementary figure 5:** Calculation of the flow rate  $Q$  by comparing between time instants the volume of fluid at either side of the hydraulic plug delimited by the cell-wall contact.

### Friction with the capillary wall

In agreement with previous related studies [24, 37], we assume that the rheology of the frictional interaction at the cell-capillary interface is viscous and linearly dependent on the normal pressure. Thus, the frictional traction is proportional to the relative sliding velocity, whose longitudinal and azimuthal components are  $\dot{z}$  and  $\rho\dot{\psi}$ , with a coefficient  $\mu_{\text{wall}}$  proportional to the normal pressure  $\mathcal{V}'(\rho)$  and given by  $\mu_{\text{wall}} = \bar{\mu}\mathcal{V}'(\rho)$ . Thus, we can write the corresponding dissipation potential as

$$W_{\text{wall}}[\dot{z}, \dot{\psi}; \rho] = \int_{\Gamma} \frac{\bar{\mu}\mathcal{V}'(\rho)}{2} [\dot{z}^2 + (\rho\dot{\psi})^2] dS_0.$$

Note that at the locations where  $\rho < r$ , the normal pressure is zero and there is no frictional interaction. The longitudinal and azimuthal frictional tractions are given by

$$t_z = \frac{\delta W_{\text{wall}}}{\delta \dot{z}} = \mu\mathcal{V}'(\rho)\dot{z}, \quad t_{\psi} = \frac{\delta W_{\text{wall}}}{\delta(\rho\dot{\psi})} = \mu\mathcal{V}'(\rho)\rho\dot{\psi}.$$

### Hydraulic resistance

As the cells move in capillary confinement, they perturb the viscous fluid around them and dissipate energy. We can distinguish between local flows around the shape-changing cells and induced flow rates along the water column in the capillary. A direct scaling argument shows that the latter should be dominant in setting fluid forces onto the cell, and for this reason we only consider the viscous dissipation due to the induced flow rate in the capillary. Recalling the expression for  $F_{\text{fluid}}$  in Supplementary Note 4, the associated dissipation potential is

$$W_{\text{fluid}}[\dot{\rho}, \dot{z}; \rho, z] = \frac{\zeta}{2\pi} Q^2.$$

Since confined cells act as hydraulic plugs and are nearly incompressible, the flow rate  $Q$  can be computed as the rate of change of volume on either side of the cell-wall contact, see Supplementary Fig. 5. This volume depends on  $\rho$  and  $z$ , and therefore its rate is a linear functional of  $\dot{\rho}$  and  $\dot{z}$ .

### Motor activity

Models for molecular motors relate forces to velocities. In the present context, the “force” is a shear force per unit length along the strip direction, denoted by  $\tau$ , opposing motor activity. The “velocity” is the sliding velocity between adjacent strips  $v_{\text{motor}}$ , obtained as pellicle shear rate times the strip width,  $v_{\text{motor}} = w\dot{\gamma}$ . In the absence of precise information about the nature, arrangement and constitutive relation of the motors powering the pellicle, we adopt an affine relation between  $v_{\text{motor}}$  and  $\tau$ , Fig. 4(a)iii [30, 31]. This affine relation is characterized by a force-free velocity  $v_{\text{motor}}^0$  and by a stall force  $\tau_{\text{stall}}$ . To model motor activation, we assume that  $v_{\text{motor}}^0$  is modulated in space and time, consistent with a control of the rate of ATP hydrolysis by the local calcium concentration. We further assume that the space-time pattern of activation  $v_{\text{motor}}^0(s, t)$ , Fig. 4(a)ii, is a time-periodic given function consistent with the shape dynamics of metaboly in the absence

of confinement [7], which can switch sign, and that the magnitude of the stall force  $\tau_{\text{stall}}$  remains constant. Such a model can be mathematically expressed as

$$v_{\text{motor}} = v_{\text{motor}}^0 \left[ 1 - \left( \text{sign } v_{\text{motor}}^0 \right) \frac{\tau}{\tau_{\text{stall}}} \right],$$

or inverting this relation as

$$\tau = \left( \text{sign } v_{\text{motor}}^0 \right) \tau_{\text{stall}} \left( 1 - \frac{v_{\text{motor}}}{v_{\text{motor}}^0} \right). \quad (48)$$

These equations show that for a given force  $\tau$  and when motors are barely activated (very small  $v_{\text{motor}}^0$ ), then the sliding velocity will also be very small, consistent with the notion that inactive motors remain in a bound state as in the flagellar axoneme [17]. In fact, in the limit  $v_{\text{motor}}^0 = 0$ , the force-velocity relation becomes the constraint  $v_{\text{motor}} = 0$  and  $\tau$  the corresponding Lagrange multiplier.

The constitutive model in Eq. (48) can be derived from an activity potential (a power per unit length)  $a(v_{\text{motor}}, v_{\text{motor}}^0)$  as

$$\tau = - \frac{\partial a}{\partial v_{\text{motor}}}$$

with

$$a(v_{\text{motor}}, v_{\text{motor}}^0) = \left( \text{sign } v_{\text{motor}}^0 \right) \tau_{\text{stall}} \left( \frac{v_{\text{motor}}^2}{v_{\text{motor}}^0} - v_{\text{motor}} \right).$$

This activity potential is quadratic and convex for any value of  $v_{\text{motor}}^0$ , and it is minimized when  $v_{\text{motor}} = v_{\text{motor}}^0$ , which will only be realized when the net force along the motor system due to other physical mechanisms vanish. Thus, within the variational modeling approach adopted here, the activity of the molecular motors can be understood in terms of a dissipation potential whose minimizer is biased biologically. Recalling the relation between sliding velocity  $v_{\text{motor}}$  and pellicle shear rate  $\dot{\gamma}$ , the total activity potential over the entire pellicle is then given by

$$W_{\text{motor}}[\dot{\gamma}; v_{\text{motor}}^0] = \int_{\Gamma} \frac{1}{w} a(w\dot{\gamma}, v_{\text{motor}}^0) dS_0,$$

where  $w$  is the strip width.

## Rayleighian and governing equations

Collecting all energy contributions, we have

$$E(X) = E_{\text{elastic}}[\rho, z, \psi, \gamma] + E_{\text{volume}}[\rho, z] + E_{\text{contact}}[\rho].$$

Therefore, the rate of change of energy can be computed from the functional derivative of  $E$

$$\dot{E} = \frac{\delta E}{\delta X}(X) \cdot \dot{X} = \delta E(\dot{X}; X).$$

We also collect all dissipative/active contributions in

$$W(\dot{X}; X, t) = W_{\text{wall}}[\dot{z}, \dot{\psi}; \rho] + W_{\text{fluid}}[\dot{\rho}, \dot{z}; \rho, z] + W_{\text{motor}}[\dot{\gamma}; v_{\text{motor}}^0].$$

We then form the Rayleighian of the system as [39, 40]

$$R(\dot{X}; X, t) = \frac{\delta E}{\delta X}(X) \cdot \dot{X} + W(\dot{X}; X, t).$$

The dynamics of the system is then given by the minimization of the Rayleighian with respect to  $\dot{X}$

$$\dot{X} = \arg \min_{\dot{X}} R(\dot{X}; X, t),$$

subject to geometric boundary conditions such as  $\rho(0, t) = \rho(1, t) = z'(0, t) = z'(1, t) = 0$ . The stationarity conditions  $\delta_{\dot{X}}R = 0$  provide a system of nonlinear partial differential equations governing the time evolution of the system. Stationarity conditions with respect to the deformation  $\{\rho, z, \psi\}$ , that is  $\delta_{\dot{\rho}}R = \delta_{\dot{z}}R = \delta_{\dot{\psi}}R = 0$ , provide the mechanical equilibrium equations in the radial, longitudinal and azimuthal directions, balancing in-plane and bending elastic stresses, contact and frictional forces, the cell pressure resulting from the volume penalty and the hydrodynamic resistance. On the other hand,  $\delta_{\dot{\gamma}}R = 0$  provides a statement of balance between actively generated forces at the pellicle strips and the forces acting externally on the motor system.

### Force balance along the capillary axis

As a particular case, global force balance along the capillary axis can be obtained by equating to zero the variation of the Rayleighian with respect to a rigid motion along  $z$ ,

$$0 = \left. \frac{d}{d\varepsilon} \right|_{\varepsilon=0} R(\dot{\rho}, \dot{z} + \varepsilon, \dot{\psi}, \dot{\gamma}; X).$$

Since all energetic contributions and the activity potential are invariant with respect to rigid body motions, this equation leads to only two contributions balancing the frictional force with the wall and the hydraulic force

$$0 = \bar{\mu} \int_{\Gamma} \mathcal{V}'(\rho) \dot{z} dS_0 + \zeta r^2 Q,$$

where the first term is the integral over the surface of the frictional traction  $t_z$  and the second term is  $F_{\text{fluid}}$ .

In the limit of large frictional coupling relative to the hydraulic resistance, this equations becomes

$$0 = \int_{\Gamma} \mathcal{V}'(\rho) \dot{z} dS_0,$$

which when divided by the net pressure force  $\int_{\Gamma} \mathcal{V}'(\rho) dS_0$  can be interpreted as the average pellicle-wall sliding velocity in the contact region. Thus, we recover in this limit the no-sliding constraint, which determines the cell velocity independently of the parameter  $\bar{\mu}$ . In the limit of small frictional coupling relative to the hydraulic resistance, force balance becomes  $Q = 0$ , which determines the cell velocity independently of  $\zeta$  and  $r$ .

### Numerical discretization

The variational structure of the statement governing the dynamics of the system can be exploited computationally to formulate time-incremental minimization problems to advance in time. This results in nonlinearly stable implicit time-stepping schemes for the dynamics, which are very robust and efficient when combined with gradient-based optimization algorithms.

Suppose we consider discrete time-instants ( $t^n$ ,  $n = 0, 1, \dots$ ) at which we will approximate the time evolution. Suppose that we know the state of the system  $X^n$  at time  $t^n$ . Using for instance a simple backward-Euler scheme, we can approximate the time-continuous Rayleighian as

$$\frac{E(X^{n+1}) - E(X^n)}{t^{n+1} - t^n} + W\left(\frac{X^{n+1} - X^n}{t^{n+1} - t^n}; X^{n+1}, t^{n+1}\right)$$

and minimize it with respect to  $X^{n+1}$  to find the new state at time  $t^{n+1}$ . Since in this minimization  $E(X^n)$  is a constant, we can rewrite the time-discrete Rayleighian as

$$R_{\Delta t}(X, X^n, t^{n+1}) = E(X) + \Delta t W\left(\frac{X - X^n}{\Delta t}; X, t^{n+1}\right)$$

where we have introduced the shorthand notation  $\Delta t = t^{n+1} - t^n$ . The time-stepping algorithm is then given by the time-incremental minimization principle

$$X^{n+1} = \arg \min_X R_{\Delta t}(X, X^n, t^{n+1}). \quad (49)$$

Having a time-discrete principle to derive the dynamics, we discretize all four unknown fields in space using a finite element expansion of the form

$$X(u, t) = \sum_I X_I(t) N_I(u), \quad \text{where } X_I(t) = \{r_I(t), z_I(t), \psi_I(t), \gamma_I(t)\},$$

and where  $N_I(u)$  are B-spline basis functions (cubic B-Splines in our calculations). The high degree of continuity of the B-Spline basis functions is required to deal with the bending elastic energy, which involves the mean curvature and hence second derivatives of the curve parametrization. Plugging this representation into  $R_{\Delta t}(X, X^n, t^{n+1})$ , Eq. (49) becomes an algebraic minimization problem that can be solved efficiently with gradient-based methods. The calculation of the gradient of the objective function is explicit and follows from the chain rule. Integrals are approximated using Gaussian quadrature in the knot spans of the B-Splines.

## Selection of model parameters

The model parameters not related to capillary confinement are the pellicle stretching modulus  $Y$ , its bending modulus  $D$ , the cell compressibility modulus  $K$ , the space-time pattern of actuation  $v_{\text{motor}}^0(s, t)$  and the stall force per unit length  $\tau_{\text{stall}}$ . Since a mechanical and biophysical characterization of the pellicle is lacking, we performed rough estimations of these parameters. Our results, however, are largely insensitive to these choices as discussed below.

The stretching modulus was computed assuming a Young's modulus for the pellicle material of about 10 MPa, typical of proteinaceous materials, and multiplying it by a nominal thickness of 40 nm, resulting in  $Y = 400 \text{ nN}/\mu\text{m}$ . Taking into account the geometry of cross-sections of the strips [1], we estimated the bending modulus as  $D = 5 \text{ nN}\cdot\mu\text{m}$ , about 100 times higher than that of a lipid bilayer.

As discussed in the main text,  $v_{\text{motor}}^0(s, t)$  was inferred from the shape dynamics of unconfined cells [7], with a maximum sliding velocity of about  $v_{\text{max}} = 0.5 \mu\text{m}/\text{s}$ . To estimate  $\tau_{\text{stall}}$ , we reasoned that, with our affine force-velocity relation, the maximum power generated per unit length in a pellicle strip interface is  $v_{\text{max}}\tau_{\text{stall}}/4$ . If we denote by  $\phi$  the number of motors per unit length, we can estimate the maximum power required from a single motor protein as

$$P = \frac{v_{\text{max}}\tau_{\text{stall}}}{4\phi}.$$

The typical step length for motors running along microtubules is  $\delta = 8 \text{ nm}$ , for which they hydrolyze a single ATP molecule. Assuming that 50% of the chemical energy is converted into mechanical energy, about  $\Delta G = 40 \text{ pN nm}$  can be extracted per step. Thus, at maximum sliding velocity, the mechanical power produced by a single molecular motor is about

$$P = \frac{\Delta G v_{\text{max}}}{\delta}.$$

Equating these two expressions, we obtain

$$\tau_{\text{stall}} = \frac{4\phi\Delta G}{\delta}.$$

Assuming that motors bridge a pair of microtubules across the interface between adjacent strips, and that  $\phi$  is one motor per 25 nm as in the axoneme, we find that  $\tau_{\text{stall}} \approx 1 \text{ nN}/\mu\text{m}$ .

With these parameters and adjusting the compressibility modulus  $K$  so that cell volume variations are below 1%, the model reaches a limit cycle that very closely resembles metaboly in the absence of confinement, with total area changes below 2%. If  $Y$  is reduced, then area changes progressively become larger and become inconsistent with our observations. If  $D$  is reduced by an order of magnitude, then the pellicle exhibits buckling events during the gait, characterized by sudden shape transitions, not observed in our experiments. If  $D$  is increased by an order of magnitude, then the shape changes are smeared by the energetic cost of bending the pellicle and the bulge cannot adopt the sharp features observed experimentally.

When placed in capillary confinement, the thickness  $\delta$  and stiffness  $k$  of the repulsive contact potential are adjusted so that the pellicle surface moves beyond the nominal capillary radius by less than 2%.

As discussed above, in the limit of high friction, the results do not depend on  $\bar{\mu}$ . Analogously, in the limit of high hydraulic resistance, the results do not depend on  $\zeta$ . We analyzed the competition between friction and hydraulic resistance by choosing the friction coefficient so that  $\mu_{\text{wall}} = \bar{\mu}\mathcal{V}'(\rho)$  agrees with our measurements reported in Supplementary Note 2, and evaluating  $\zeta$  for our capillary geometry. We found that the results closely followed the limit of high hydraulic resistance, in agreement with the results reported in Fig. 3.

## Supplementary Note 6

### Confined metaboly in *Distigma proteus* and *Peranema trichophorum*

To test the generality of our observations, we first examined *Distigma proteus*, a primary osmotrophic species thought to have a phagotropic ancestor and exhibiting pronounced metaboly. We found that these cells swam using their flagella when unconfined. As for *Euglena gracilis*, confinement between two plates triggered non-reciprocal peristaltic cell deformations, which allowed *Distigma* cells to crawl at speeds of about  $0.41 \pm 0.04$  body lengths per cycle (standard error of the mean,  $n=4$ ), see Supplementary Movie S14. We then examined *Peranema trichophorum*, a voracious phagotroph known to engulf very large prey thanks to cell body deformations. In the absence of confinement, these cells glided on the substrate thanks to movements of the tip of their visible propulsive flagellum [41]. During gliding, they occasionally changed shape, including bending of their body in a coordinated movement that also involved a change in the gait of the flagellum and that resulted in sharp turns of their trajectory [42]. Under high confinement between two glass plates, *Peranema* cells were not able to glide and consistently developed periodic shape changes, see Supplementary Movie S15. However, in contrast with those of *Euglena* or *Distigma* cells, these shape changes were less specific, largely reciprocal, and did not accomplish significant net motion.

Thus, a minimal examination of metaboly across euglenids suggests that species endowed with a deformable pellicle can operate this motile machinery in various ways, possibly accomplishing different functions. *Peranema* cells, phagotrophs as the ancestor of all cells examined here, use it to engulf large objects and to bend their body during turns while gliding. *Euglena* and *Distigma* cells, which do not use metaboly for phagotrophy, develop a remarkably non-reciprocal version of metaboly under confinement, which enables fast and versatile crawling. Our computational model shows that these different modes of operation of the pellicle only require different space-time activation patterns, which suggests that functional innovations of the pellicle do not require modifications of the complex cortical system but rather changes in the signaling networks that determine pellicle activation in space and time. The broader implications of this observation will be the subject of future studies.

## Captions of Supplementary Movies

**Supplementary Movie S1:** Video recordings of *Euglena gracilis* between glass slides separated by a spacer of thickness  $\sim 80 \mu\text{m}$ . In dilute cultures (left), cells exhibit flagellar swimming without cell shape changes. In crowded cultures (right), cells display a variety of behaviors, including flagellar swimming, cell rounding and spinning, and large amplitude periodic cell body deformations typical of metaboly.

**Supplementary Movies S2 and S3:** *Euglena gracilis* cells exhibiting metaboly and directed motion in the anterior-to-posterior direction while confined between glass slides. Observation using brightfield reflected light microscopy reveals the reconfigurations of the striated cell envelope concomitant with cell body deformations in the plane of the glass slide. The separation between the slides is  $\sim 6 \mu\text{m}$  and  $\sim 4 \mu\text{m}$  for Supplementary Movie S2 and S3, respectively.

**Supplementary Movie S4:** Video recordings of *Euglena gracilis* in tapered capillaries. Cells swimming into tapered capillaries transition from flagellar swimming (top left) to developing large amplitude shape excursions (top right), including rounding (bottom left). When confined in capillary diameters smaller than about twice the free-swimming cell diameter, most cells develop the prototypical peristaltic cell body deformations of metaboly (bottom right).

**Supplementary Movie S5:** *Euglena gracilis* cell confined in a glass capillary and imaged using brightfield reflected light microscopy. Rounding of the cell body, as determined by the reconfigurations of the pellicle strips, allows the cell to switch its orientation. The microscope was intermittently focused at the pellicle-capillary interface to visualize the pellicle and at the capillary axis to visualize cell shape.

**Supplementary Movie S6:** Video recordings of *Euglena gracilis* exhibiting metaboly and directed motion in tapered capillaries under increasing confinement, as quantified by ratio of  $d_{\text{cap}}/d_{\text{cell}}$ , along with kymographs relative to the capillary axis. The movie shows that crawling by metaboly is effective up to very large degree of confinement.

**Supplementary Movie S7:** Video recordings of *Euglena gracilis* not exhibiting body deformations and acting as hydraulic plugs driven by a known pressure difference,  $p_{\text{in}}$ , of increasing magnitude between the capillary extremities. Data from these experiments allowed us to quantify a viscous and confinement-dependent friction between cells and the capillary walls.

**Supplementary Movie S8:** Video recordings of *Euglena* cells stuck in a glass capillary and beating their anterior flagellum.

**Supplementary Movie S9:** Results from the idealized model for the power phase of metaboly in the limit of infinite wall friction relative to hydraulic resistance (top), in the limit of zero wall friction relative to hydraulic resistance (bottom), and for an intermediate case where hydraulic propulsive forces and frictional resistive forces compete (middle). The blue arrows report the average fluid velocity induced by the cell, defined as the flow rate divided by the cross-sectional area of the capillary. The surface of the idealized model is decorated along slip lines by material particles to highlight their motion relative to the capillary walls in the contact region.

**Supplementary Movie S10:** Video recordings of an *Euglena* cell effectively crawling by metaboly (right) in the presence of a immobile cell, stuck in the capillary and acting as a hydraulic plug (left).

**Supplementary Movie S11:** Video recordings of *Euglena gracilis* performing metaboly in a capillary and of suspended polystyrene beads by combining brightfield and fluorescence microscopy. Data from these experiments allowed us to quantify the fluid flow around crawling cells by tracking the fluorescent beads.

Only beads in the vicinity of the cell undergo rapid motions due to local flows induced by shape changes and flagellar beating.

**Supplementary Movie S12:** *Euglena gracilis* crawling by metaboly while confined into a glass capillary. Observation using brightfield reflected light microscopy allows for the visualization of the pellicle strips in contact with the capillary wall. The microscope was intermittently focused at the pellicle-capillary interface to visualize the pellicle and at the capillary axis to visualize cell shape. The movie reports also the kymograph relative to the capillary axis. The trajectories of pellicle features reveal sliding between the pellicle and the capillary wall in the contact region.

**Supplementary Movie S13:** Computational results from the theoretical model of crawling by metaboly under confinement. Results are shown for increasing confinement, as quantified by ratio of  $d_{\text{cap}}/d_{\text{cell}} = \{0.875, 1.0, 1.375, 1.8\}$ , in the limit of high hydraulic resistance, and during three cycles. The cell motion is reported by black and white features fixed in the frame of the capillary. Notice that the model self-adapts to imposed confinement by developing a limit cycle (gait), which is consistent with the experimental observations on *Euglena* cells. The four gaits at different degrees of confinement are the result on the same activation pattern, represented as a space-time colormap (left).

**Supplementary Movie S14:** Video recordings of *Distigma proteus* between glass slides separated on one side by a spacer of thickness  $\sim 80 \mu\text{m}$  in order to realize a wedge-shaped fluid chamber. In the absence of confinement (gap between plates  $\sim 36 \mu\text{m}$ ), cells exhibit flagellar swimming. Significant confinement between the two plates (gap  $\sim 5 \mu\text{m}$ ) triggers non-reciprocal peristaltic cell deformations, which allow *Distigma* cells to crawl.

**Supplementary Movie S15:** Video recordings of *Peranema trichophorum* between glass slides separated on one side by a spacer of thickness  $\sim 80 \mu\text{m}$  in order to realize a wedge-shaped fluid chamber. In the absence of confinement (gap between plates  $\sim 52 - 43 \mu\text{m}$ ), cells glide on the substrate thanks to the movement of their flagellum. During gliding, cells occasionally bend their body, and this shape change is associated with sharp turns of the cell trajectory. Under high confinement between the glass plates (gap  $\sim 7 \mu\text{m}$ ), cells are not able to glide and develop periodic, largely reciprocal shape changes.

## Supplementary References

- [36] do Carmo, M. P. *Differential geometry of curves and surfaces*. Prentice-Hall, Englewood Cliffs (1976).
- [37] Klein, J. Hydration lubrication. *Friction* **1**, 1-23 (2013).
- [38] Kim, S. & Karrila, S. J. *Microhydrodynamics: Principles and Selected Applications*. Courier Corporation, Mineola (2013).
- [39] Doi, M. Onsager's variational principle in soft matter. *J. Phys.: Condens. Matter* **23**, 284118 (2011).
- [40] Arroyo, M., Walani, N., Torres-Sánchez, A. & Kaurin, D. Onsager's variational principle in soft matter: Introduction and application to the dynamics of adsorption of proteins onto fluid membranes. In: Steigmann, D. J. (ed) *The Role of Mechanics in the Study of Lipid Bilayers* Springer International Publishing, Cham (2018).
- [41] Saito, A. et al. Gliding movement in *Peranema trichophorum* is powered by flagellar surface motility. *Cell Motil. Cytoskeleton* **55**, 244-253 (2003).
- [42] Chang, S. L. Observations on the organelles, movement, and feeding of *Peranema trichophorum* (Ehrb.) Stein. *T. Am. Microsc. Soc.* **85**, 29-45 (1966).